nature materials

ARTICLES

https://doi.org/10.1038/s41563-021-01114-z

Check for updates

Three-dimensional atomic packing in amorphous solids with liquid-like structure

Yakun Yuan[1,5], Dennis S. Kim[1,5], Jihan Zhou[1,5], Dillan J. Chang[1], Fan Zhu[1], Yasutaka Nagaoka[2], Yao Yang[1], Minh Pham[3], Stanley J. Osher[3], Ou Chen[2], Peter Ercius[4], Andreas K. Schmid[4] and Jianwei Miao[1]✉

Liquids and solids are two fundamental states of matter. However, our understanding of their three-dimensional atomic structure is mostly based on physical models. Here we use atomic electron tomography to experimentally determine the three-dimensional atomic positions of monatomic amorphous solids, namely a Ta thin film and two Pd nanoparticles. We observe that pentagonal bipyramids are the most abundant atomic motifs in these amorphous materials. Instead of forming icosahedra, the majority of pentagonal bipyramids arrange into pentagonal bipyramid networks with medium-range order. Molecular dynamics simulations further reveal that pentagonal bipyramid networks are prevalent in monatomic metallic liquids, which rapidly grow in size and form more icosahedra during the quench from the liquid to the glass state. These results expand our understanding of the atomic structures of amorphous solids and will encourage future studies on amorphous–crystalline phase and glass transitions in non-crystalline materials with three-dimensional atomic resolution.

In 1952, Frank hypothesized that icosahedral order is the prevalent atomic motif in monatomic liquids[1]. Over the past six decades, there have been a great deal of experimental, computational and theoretical studies to understand the structure of liquids and amorphous materials[2–23]. A polytetrahedral packing model has been proposed to explain the three-dimensional (3D) atomic structure of monatomic liquids and amorphous materials[24], in which icosahedral order is a key feature. The icosahedral order has also been found to play a critical role in the structure of metallic glasses and quasicrystals[25–31]. Despite all these developments, however, no experimental method could directly determine the 3D atomic packing of liquids and amorphous materials due to the lack of long-range order. Atomic electron tomography (AET), allowing the determination of the 3D atomic structure of materials without assuming crystallinity[32], is uniquely positioned to address this challenge. Since its first demonstration in 2012 (ref. [33]), AET has been applied to reveal a wide range of crystal defects in materials, such as grain boundaries, dislocations, stacking faults, point defects, atomic ripples, bond distortion, strain tensors and chemical order/disorder in three and four dimensions[32,34–41]. More recently, AET was used to determine the structure of a multi-component metallic glass nanoparticle and quantitatively characterize the short- and medium-range order of its 3D atomic arrangement[42]. Here we advance AET to reveal the 3D atomic structure of an amorphous Ta thin film and two amorphous Pd nanoparticles that are not metallic glasses but have a liquid-like structure. We observed that pentagonal bipyramids are the main atomic motifs in the monatomic amorphous materials. Instead of assembling icosahedra, most pentagonal bipyramids closely connect with each other to form pentagonal bipyramid networks (PBNs) that extend to the medium-range order.

AET of monatomic amorphous materials

The AET experiments were conducted with a scanning transmission electron microscope (STEM) in annular dark-field (ADF) mode. Tomographic tilt series were acquired from an amorphous Ta thin film and two Pd nanoparticles (Supplementary Table 1 and Supplementary Figs. 1–3), which were synthesized by physical vapour deposition and colloidal chemistry with ligand engineering, respectively (Methods). Images acquired before, during and after the acquisition of each tilt series indicate a minimal change of the sample structure throughout the experiment (Supplementary Fig. 4). To verify the amorphous nature of the samples, two-dimensional (2D) power spectra were calculated from the experimental images, showing the amorphous halo (insets in Supplementary Figs. 1–3). Electron diffraction experiments were also conducted to obtain the structure factors and pair distribution functions (PDFs) of the Ta film and Pd nanoparticles[43] (Methods and Supplementary Fig. 5). The PDFs confirm the amorphous nature of the samples but show no second-peak splitting, indicating that these samples are not metallic glasses[19,26].

After image preprocessing, each tilt series was reconstructed by a real space iterative algorithm, and the 3D coordinates of individual atoms were traced and refined to produce an experimental atomic model (Methods). Compared to nanoparticles[32,38,39], the AET reconstruction of thin films is more challenging as the projections at different tilt angles contain different volumes of the thin film (Supplementary Fig. 1). We have developed an advanced iterative reconstruction algorithm to solve this problem and determine the 3D atomic coordinates in the amorphous Ta thin film (Methods). The precision of the 3D atomic coordinates was determined to be 18 picometres (Supplementary Fig. 6). Figure 1a,b and Supplementary Fig. 7 show the experimental 3D atomic model of the Ta thin film and two Pd nanoparticles (named Pd_1 and Pd_2), respectively. To quantify the disorder, we calculated the bond orientational order parameters for all the atoms[44] (Methods and Supplementary Fig. 8a–c). We observed that 20.1%, 2.2% and 1.8% of the atoms form crystal nuclei on the surface of the Ta thin film and the Pd_1 and Pd_2 nanoparticles, respectively (grey atoms in Fig. 1a,b,

[1]Department of Physics and Astronomy and California NanoSystems Institute, University of California, Los Angeles, Los Angeles, CA, USA. [2]Department of Chemistry, Brown University, Providence, RI, USA. [3]Department of Mathematics, University of California, Los Angeles, Los Angeles, CA, USA. [4]National Center for Electron Microscopy, Molecular Foundry, Lawrence Berkeley National Laboratory, Berkeley, CA, USA. [5]These authors contributed equally: Yakun Yuan, Dennis S. Kim, Jihan Zhou. ✉e-mail: miao@physics.ucla.edu

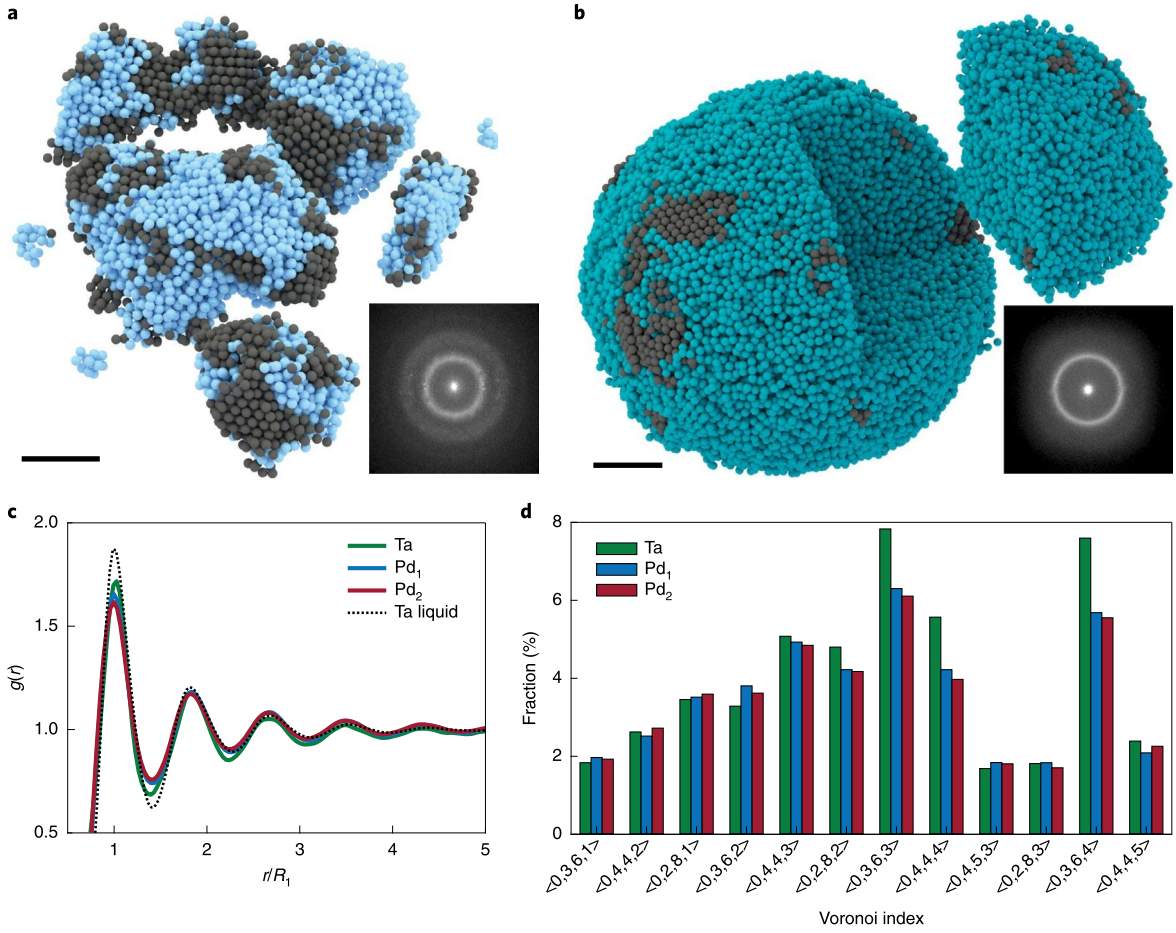

Fig. 1 | Determination of the 3D atomic structure of monatomic amorphous materials. a,**b**, Experimental 3D atomic model of an amorphous Ta film (**a**) and a Pd nanoparticle (Pd_1; **b**) with surface crystal nuclei in grey. The two insets show the average 2D power spectra of the experimental images for the Ta film and Pd_1 nanoparticle, where the amorphous halo is visible. Scale bars, 2 nm. **c**, PDFs of the Ta film (green), two Pd nanoparticles (Pd_1 in blue and Pd_2 in red) and an MD-simulated Ta liquid at 5,200 K (dotted curve), where $g(r)$ is the PDF and r/R_1 is the distance (r) normalized by the first peak position (R_1). **d**, The 12 most populated Voronoi polyhedra in the three samples, where the Voronoi index is arranged with the increase of the coordination number. All the analyses in **c** and **d** and Figs. 2–6 are based on the amorphous regions of the three samples with the crystal nuclei removed.

Supplementary Fig. 7a and Supplementary Videos 1–3). After excluding these nuclei, we plot the PDFs of the disordered atoms (Fig. 1c), which exhibit similar shapes despite the different chemical composition and synthesis methods of the samples. As a comparison, the PDF of a Ta liquid obtained by the molecular dynamics (MD) simulation is shown as a dotted curve in Fig. 1c, in which the peak and valley positions agree with those of the Ta thin film and two Pd nanoparticles.

Next, we quantified the 3D short-range atomic packing of the samples using the Voronoi tessellation[4,25]. This method characterizes each local polyhedron around a centre atom by calculating a Voronoi index, $<n_3,n_4,n_5,n_6>$, where n_i denotes the number of i-edged faces (Methods). Figure 1d shows the 12 most populated Voronoi polyhedra in the three samples. We found that distorted icosahedra with <0,0,12,0>, <0,1,10,2>, <0,2,8,2> and <0,2,8,1> account for 9.8% in the three samples. By contrast, among all the faces in the Voronoi polyhedra (Supplementary Fig. 8d), five-edged faces are the most abundant (45.5%), indicating that the majority of five-edged faces do not form distorted icosahedra. From the Voronoi indices, we determined the average coordination number of the Ta, Pd_1 and Pd_2 samples to be 12.2, 12.3 and 12.3, respectively, which agree well with that of monatomic liquids (12 ± 1) measured from diffraction experiments[45].

Polytetrahedral packing in monatomic amorphous materials

To quantitatively characterize the tetrahedra in the amorphous materials (Methods), we used the distortion parameter[15,46], defined as $\delta = e_{max}/e_{avg} - 1$, where e_{max} and e_{avg} are the maximum and average edge lengths of each tetrahedron, respectively. Supplementary Fig. 9 (green curves) shows the fraction of the tetrahedra as a function of δ. With $\delta > 0.2$, more than 96.8% of the atoms in the samples form tetrahedra. By sharing faces, these tetrahedra constitute four main motifs: triplets, quadrilateral, pentagonal and hexagonal bipyramids (Fig. 2a). The four motifs are represented by three-, four-, five- and six-fold skeletons, which are formed by connecting the centroids of the tetrahedra (coloured lines in Fig. 2a). Figure 2b and Supplementary Fig. 9 show the fraction of the four motifs as a function of δ. With $\delta < 0.2$, the tetrahedra are not fully packed in 3D space, leading to a dominant fraction of triplets. With the increase of δ, the quadrilateral, pentagonal and hexagonal bipyramids increase, while the triplets decrease. In the following analysis, we choose $\delta \leq 0.255$, which was previously used in mathematical and numerical simulation studies[15,46]. Figure 2c shows the population of the four motifs in the three samples, indicating that pentagonal bipyramids are the most abundant atomic motif. This observation is consistent with the Voronoi tessellation analysis (Supplementary Fig. 8d) and

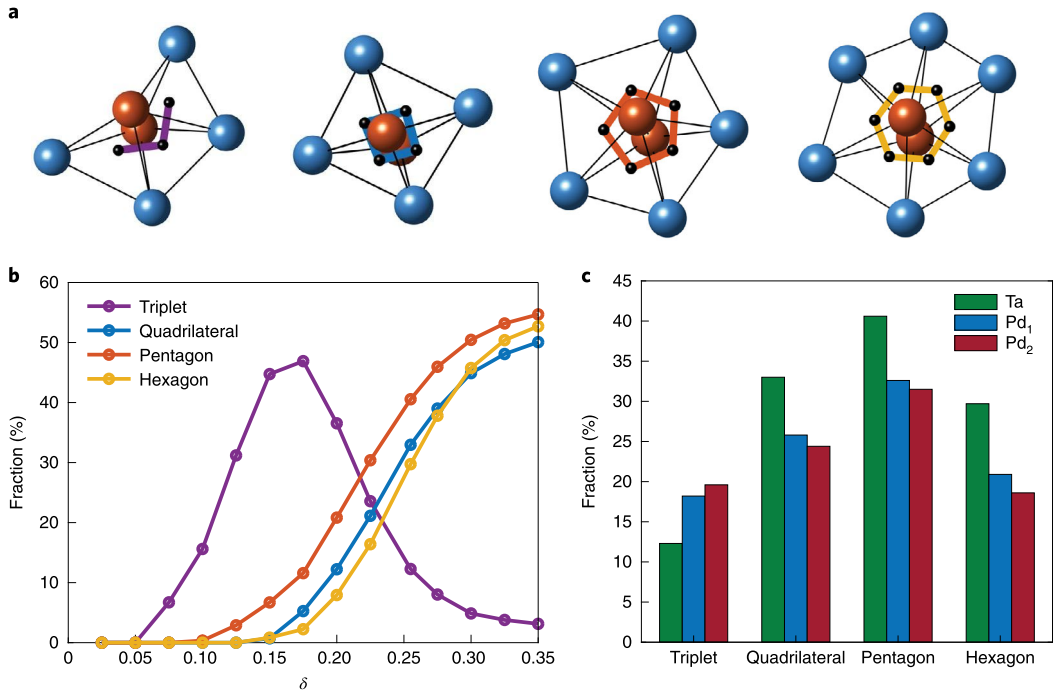

Fig. 2 | Polytetrahedral packing in the amorphous Ta film and two Pd nanoparticles. a, The four most populated atomic motifs (triplets, quadrilateral, pentagonal and hexagonal bipyramids) in the three samples, where the capping atoms are in brown and the ring atoms are in blue, connected by the bonds (black lines). The four motifs are represented by a three- (purple), four- (blue), five- (orange) and six-fold (yellow) skeleton, which connects the centroid (black dot) of each tetrahedron. **b**, Population of the four atomic motifs in the Ta film as a function of δ. **c**, Distribution of the four atomic motifs in the amorphous Ta film (green) and Pd_1 (blue) and Pd_2 (red) nanoparticles with $\delta \leq 0.255$.

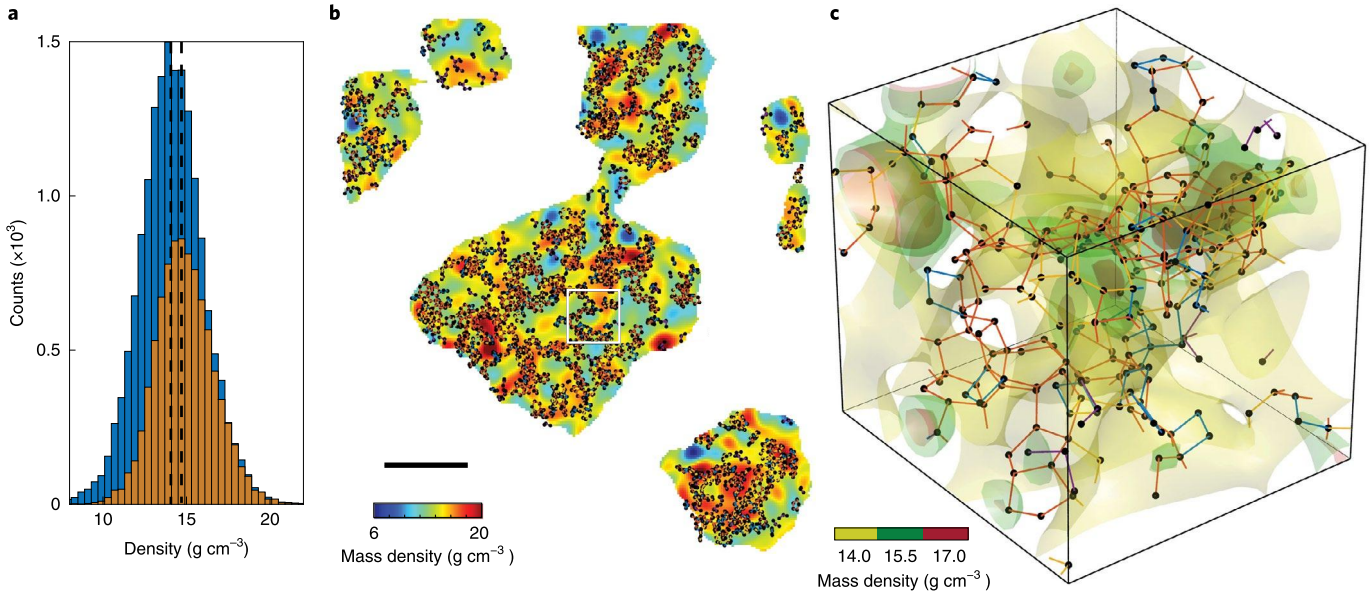

Fig. 3 | Correlation of 3D local mass density heterogeneity and polytetrahedral packing. a, Mass density distribution in the regions of the amorphous Ta film with (orange) and without (blue) polytetrahedral packing, where polytetrahedral packing increases the average mass density by 3% (dashed lines). **b**, A slice through the Ta film shows the local mass density heterogeneity (colour) overlaid with polytetrahedral packing (black). Scale bar, 2 nm. **c**, A 3D surface rendering of local mass density heterogeneity magnified from the square region in **b**, which is overlaid with three- (purple), four- (blue), five- (orange) and six-fold (yellow) skeletons.

can be explained by the fact that the atomic packing in pentagonal bipyramids requires less distortion than in the other motifs[24,26].

Since a tetrahedron and a pentagonal bipyramid represent the densest packing of four and seven atoms[24], respectively, we correlated polytetrahedral packing with the local mass density of the amorphous materials (Methods). Figure 3a and Supplementary Fig. 10a,d show the mass density distribution in the regions of three samples with and without polytetrahedral packing, where the

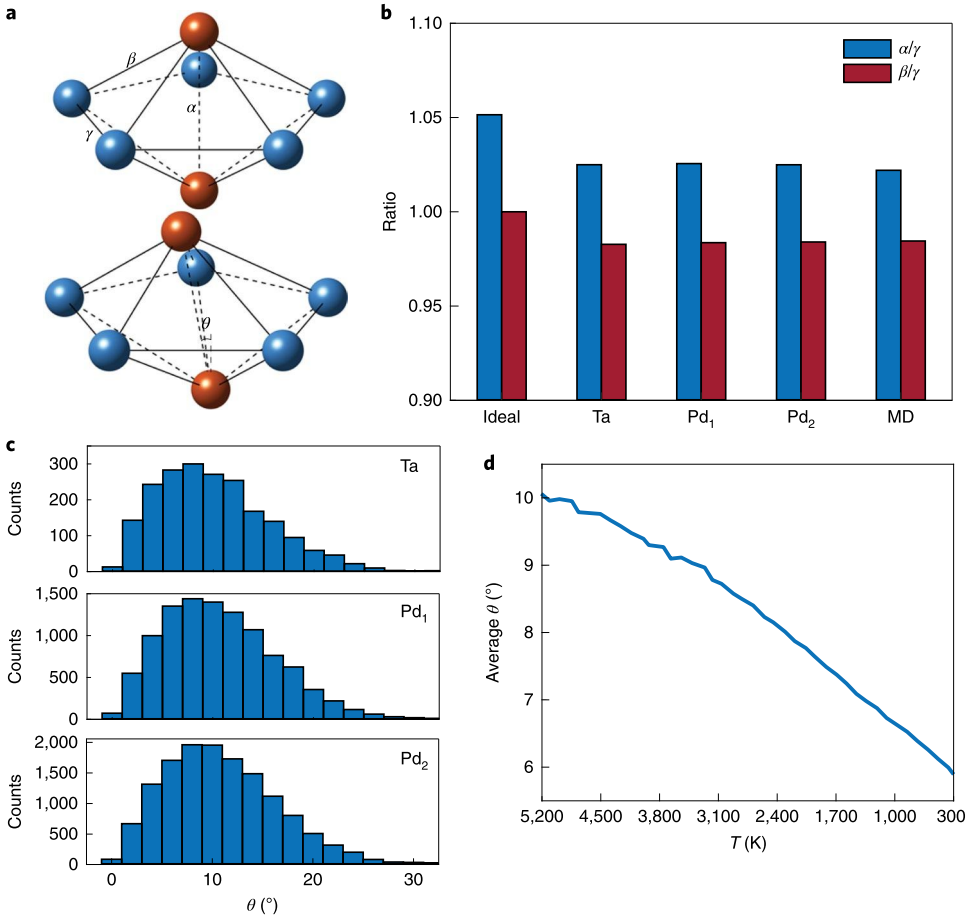

Fig. 4 | Quantitative characterization of 3D atomic packing of pentagonal bipyramids. a, An ideal pentagonal bipyramid (top) consisting of two capping (brown) and five ring (blue) atoms. The α, β and γ represent the capping, capping–ring and ring atom bonds, respectively. The bottom shows the average pentagonal bipyramid of the amorphous Ta film, where the α bond and the plane of five ring atoms form an angle (θ). **b**, The α/γ and β/γ ratios of an ideal pentagonal bipyramid as well as those in the amorphous Ta film, Pd_1 and Pd_2 nanoparticles, and MD-simulated Ta liquid at 5,200 K. **c**, Distribution of θ in the Ta film (top) and Pd_1 (middle) and Pd_2 (bottom) nanoparticles with the average θ of 10.0°, 10.7° and 10.9°, respectively. **d**, Average θ as a function of the temperature during the quench of Ta from the liquid to the metallic glass state.

average mass density increases with polytetrahedral packing. We also observed 3D local mass density heterogeneity in the amorphous materials. A slice through each sample shows the local mass density heterogeneity overlaid with polytetrahedral packing (Fig. 3b and Supplementary Fig. 10b,e). A magnified region in each sample reveals that 3D local mass density heterogeneity is strongly correlated to the atomic packing of the four motifs in the three samples (Fig. 3c and Supplementary Fig. 10c,f).

As pentagonal bipyramids are the most abundant motif, we quantified their 3D atomic packing in the three amorphous materials. Supplementary Fig. 11a–c shows the bond angle distributions of the Ta film and Pd_1 and Pd_2 nanoparticles, respectively, which agree with the previous study of metallic liquids using reverse Monte Carlo simulations[13]. The two peaks of the bond angle distribution are consistent with the internal angle of a tetrahedron and a pentagon, respectively (Supplementary Fig. 11d). Next, we quantified the three bonds in the pentagonal bipyramid: the capping atom bond (α), the capping–ring atom bond (β) and the ring atom bond (γ; Fig. 4a, top). According to the polytetrahedral packing model[24,26], an ideal pentagonal bipyramid consisting of seven atoms has the α bond 5% longer than the β and γ bonds. However, we found that the α bond is statistically 2.5% longer than the γ bond and the β bond is 1.3% shorter than the γ bond in the three amorphous samples (Fig. 4b). We also observed that the angle (θ) between the α bond and the plane of five ring atoms (Fig. 4a, bottom) deviates from an ideal pentagonal bipyramid of $\theta = 0°$. Figure 4c shows that the average θ was measured to be 10.0°, 10.7° and 10.9° for the amorphous Ta film and Pd_1 and Pd_2 nanoparticles, respectively. All these results indicate that the pentagonal bipyramids are distorted in these amorphous samples. The same distortion was also observed in the MD-simulated Ta liquid (Methods). As the liquid is quenched from 5,200 K to 300 K, θ decreases (Fig. 4d) but the α/γ and β/γ ratios remain relatively unchanged (Fig. 4b).

The PBN

We observed that a number of pentagonal bipyramids link to each other by sharing four or five atoms with their neighbours (Fig. 5a,b), which we define as vertex or edge sharing of the five-fold skeletons, respectively. Figure 5c and Supplementary Fig. 12 show the fraction of pentagonal bipyramids as a function of the number of vertex- and edge-sharing neighbours. We found that while 63.5% of pentagonal bipyramids in the three samples do not share any vertex with their neighbours, the majority of them (72.5%) have at least one edge-sharing neighbour. Figure 5d,e shows two pentagonal bipyramid clusters with the most vertex- and edge-sharing neighbours, respectively, where the larger cluster is formed by edge sharing. These results indicate that edge sharing of the five-fold skeletons is a more dominant feature in

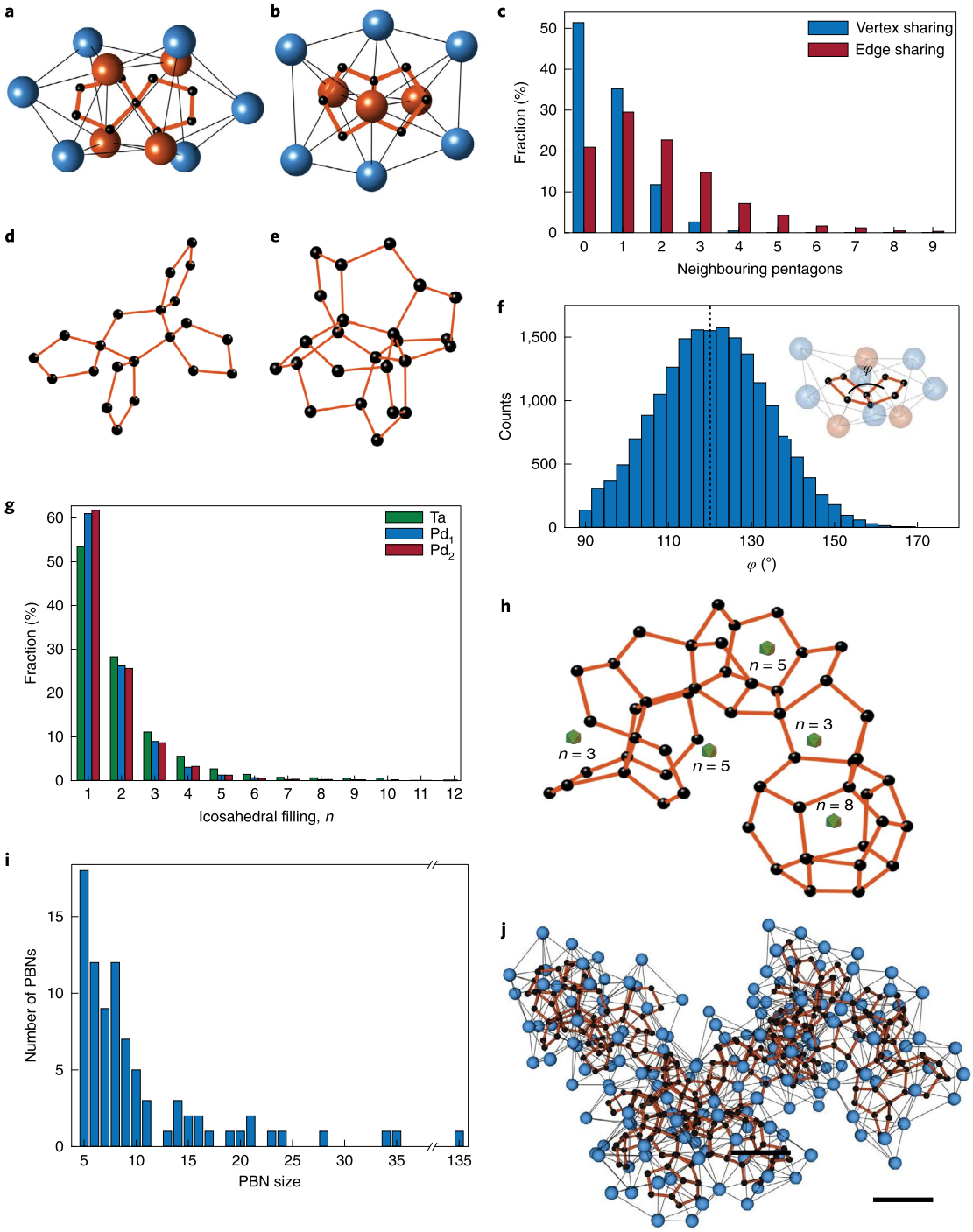

Fig. 5 | Direct observation of PBNs in monatomic amorphous materials. a,**b**, Vertex and edge sharing of the five-fold skeletons, which share four and five atoms with their neighbours, respectively. The capping atoms are in brown. **c**, Population of pentagonal bipyramids as a function of the number of vertex- and edge-sharing neighbours in the amorphous Ta film. **d**,**e**, Pentagonal bipyramid clusters with the most vertex- (**d**) and edge-sharing neighbours (**e**) in the three amorphous materials. **f**, Distribution of the dihedral angles (φ) between two edge-sharing pentagonal bipyramids (inset) in the three amorphous materials, where the average φ is 120.7° (dashed line). **g**, Population of pentagonal bipyramids filling partial icosahedral sites (n). The formation of a full icosahedron requires $n = 12$. **h**, Five-fold skeleton of a representative PBN, containing five partial icosahedra with $n = 3$, 5, 5, 3 and 8. The centre of each partial icosahedron is labelled by an icosahedron (green). **i**, Histogram of the PBNs as a function of their size (that is, the number of pentagonal bipyramids) in the Ta thin film. **j**, The largest PBN in the amorphous materials, containing 135 pentagonal bipyramids formed by 165 Ta atoms (blue balls). The black lines represent the bonds between the Ta atoms and the black dots and orange lines show the PBN with five-fold skeletons. Scale bar, 4 Å.

the packing of pentagonal bipyramids. We then investigated if these pentagonal bipyramids form icosahedra. An icosahedron requires the tight packing of 12 pentagonal bipyramids by edge sharing. Due to geometric frustration[24,29], the five-fold skeletons in an icosahedron form a regular dodecahedron with the dihedral angle (φ) of 116.57° (Fig. 5f, inset). But we observed

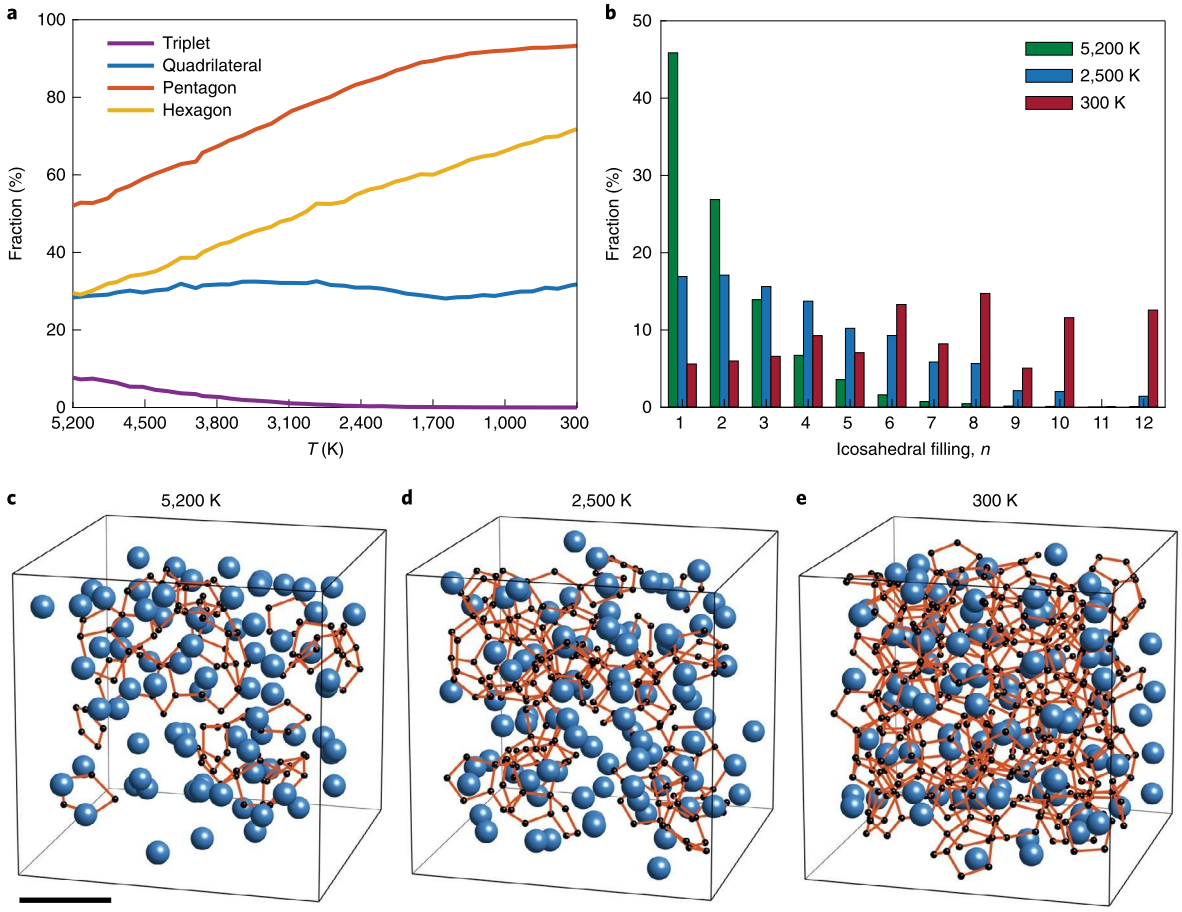

Fig. 6 | PBNs in the MD-simulated Ta liquid and metallic glass. a, Population of the four most abundant atomic motifs (triplets, quadrilateral, pentagonal and hexagonal bipyramids) as a function of the temperature. **b**, Population of pentagonal bipyramids filling partial icosahedral sites (*n*) at the liquid temperature (5,200 K), during quench (2,500 K) and at room temperature (300 K). **c**–**e**, Snapshot of a fraction of the 3D atomic models and PBNs at the above three temperatures. Ta atoms are shown as blue balls and the PBNs as orange lines and black dots. The PBNs quickly grow in size and form more icosahedra with the decrease of the temperature. Scale bar, 4 Å.

that the dihedral angles (φ) between two edge-sharing pentagonal bipyramids peak at 120.7° in the three amorphous samples (Fig. 5f), a value that is close to $\varphi = 120°$ in the absence of geometric frustration. This observation further confirms that the pentagonal bipyramids assemble only partial icosahedra (Fig. 5g). These results do not contradict that 9.8% of all the Voronoi polyhedra in the three samples are distorted icosahedra because the vast majority of these distorted icosahedra have a large distortion with $\delta > 0.255$ (Supplementary Fig. 13). When choosing $\delta \leq 0.255$, the total number of distorted icosahedra and pentagonal bipyramids in the three amorphous materials is 17 and 26,262, respectively, showing that the pentagonal bipyramids are far more abundant than the distorted icosahedra in the samples.

Instead of assembling icosahedra, most pentagonal bipyramids with edge-sharing skeletons form PBNs in the amorphous samples. Figure 5h shows a representative PBN comprising five partial icosahedra. Figure 5i and Supplementary Figs. 14 and 15 show the histograms of the PBNs as a function of their size and length, which extend to the nanometre scale. The largest PBN was found in the Ta thin film, consisting of 135 pentagonal bipyramids formed by 165 atoms with an end-to-end length of 2.83 nm (Fig. 5j). The five largest PBNs in the Ta, Pd_1 and Pd_2 samples are shown in Supplementary Figs. 16–18. Compared with the networks formed by quadrilateral and hexagonal bipyramids, the PBNs not only are more abundant, but also have a larger size in all three samples (Supplementary Figs. 14 and 15), indicating the PBNs are dominant in monatomic amorphous materials.

To investigate if PBNs are prevalent in other amorphous systems such as liquids and metallic glasses, we employed MD simulations using the large-scale atomic/molecular massively parallel simulator[47] (Methods). A bulk Ta solid was melted at 5,200 K, quenched at a cooling rate of 10^{13} K s^{-1} and brought to equilibrium at 300 K. The PDFs of the Ta structures at varying temperatures are shown in Supplementary Fig. 19. At 5,200 K, the PDF of the Ta liquid resembles those of experimentally measured amorphous materials in terms of the peak and valley positions (dotted curve in Fig. 1c). At 300 K, the second-peak splitting in the PDF indicates the formation of the Ta metallic glass[19,26] (arrows in Supplementary Fig. 19). By analysing the polytetrahedral packing of these Ta structures with $\delta \leq 0.255$, we found that pentagonal bipyramids are the most abundant atomic motif across the entire temperature range and their population dramatically increases with the decrease of the temperature (Fig. 6a). At 5,200 K, we observed PBNs and partial icosahedra in the Ta liquid (Fig. 6b,c and Supplementary Fig. 20). These PBNs extend to the medium-range order and resemble those found in the amorphous Ta thin film and two Pd nanoparticles (Fig. 5i,j and Supplementary Figs. 16–18). With the decrease of temperature, the PBNs rapidly grow in size, and a fraction of them form icosahedra (Fig. 6b,d and Supplementary Fig. 21). At 300 K, a huge PBN is created across the entire Ta metallic glass (Supplementary Fig. 21c) and

more icosahedra are formed (Fig. 6b,e). We have also performed MD simulations of quenching Pd from the liquid to the metallic glass state and observed very similar results.

Discussion and outlook

Our experimental results, coupled with MD simulations, provide fundamental insight into the 3D atomic packing of monatomic amorphous materials and liquids. Although there are several crystal nuclei on the surface of the Ta thin film and two Pd nanoparticles, we verified that the crystal nuclei have a minimal impact on the structural disorder of the samples based on the following observations. First, after quantitatively analysing the crystalline–amorphous interface in the samples (Methods), we determined the characteristic width of the interface to be around 3.0–4.3 Å (Supplementary Fig. 22), which is in accordance with the previous MD simulation result[48]. This analysis indicates that the crystal nuclei do not affect the atomic-level structural disorder beyond a few angstroms. Second, after removing the crystal nuclei, the peak and valley positions of the PDFs of the amorphous materials are in good agreement with those of the MD-simulated Ta liquid (Fig. 1c). Furthermore, the bond ratio, the bond angle and the 3D atomic packing in the amorphous Ta thin film and two Pd nanoparticles are consistent with those of the MD-simulated Ta liquid (Figs. 4–6 and Supplementary Figs. 11, 16–18 and 20). The observations demonstrate that these monatomic amorphous materials and the metallic liquid, although representing two different states of matter, have similar 3D atomic structures.

Our experimental and MD simulation results further reveal that pentagonal bipyramids are the prevalent atomic motif and form nanometre-scale PBNs in monatomic amorphous materials and liquids. During the quench from a liquid to a metallic glass state, the PBNs quickly grow in size and assemble more icosahedra, indicating the PBNs can trap the atoms in a local minimum (a non-crystalline or glass state) instead of a global minimum (a crystalline state). Looking forward, the ability to determine the 3D atomic structure of amorphous thin films is expected to greatly expand the applicability of AET to a broad range of technologically relevant materials[49]. Moreover, the experimental method and results reported in this work could have an important impact on different fields, ranging from the direct determination of the 3D atomic structure of quasicrystals[30,31] to the study of the physics of jamming[50], the amorphous–crystalline phase and glass transitions at the single-atom level[51,52].

Online content

Any methods, additional references, Nature Research reporting summaries, source data, extended data, supplementary information, acknowledgements, peer review information; details of author contributions and competing interests; and statements of data and code availability are available at https://doi.org/10.1038/s41563-021-01114-z.

Received: 15 February 2021; Accepted: 20 August 2021;
Published online: 18 October 2021

References

1. Frank, F. C. Supercooling of liquids. *Proc. R. Soc. Lond. A* **215**, 43–46 (1952).
2. Bernal, J. D. A geometrical approach to the structure of liquids. *Nature* **183**, 141–147 (1959).
3. Scott, G. D. Packing of spheres: packing of equal spheres. *Nature* **188**, 908–909 (1960).
4. Finney, J. L. Random packings and the structure of simple liquids. I. The geometry of random close packing. *Proc. R. Soc. Lond. A* **319**, 479–493 (1970).
5. Nelson, D. R. Order, frustration, and defects in liquids and glasses. *Phys. Rev. B* **28**, 5515–5535 (1983).
6. Jonsson, H. & Andersen, H. C. Icosahedral ordering in the Lennard-Jones liquid and glass. *Phys. Rev. Lett.* **60**, 2295–2298 (1988).
7. Chen, L. C. & Spaepen, F. Calorimetric evidence for the micro-quasicrystalline structure of 'amorphous' Al/transition metal alloys. *Nature* **336**, 366–368 (1988).
8. Reichert, H. et al. Observation of five-fold local symmetry in liquid lead. *Nature* **408**, 839–841 (2000).
9. Spaepen, F. Five-fold symmetry in liquids. *Nature* **408**, 781–782 (2000).
10. Kelton, K. F. et al. First X-ray scattering studies on electrostatically levitated metallic liquids: demonstrated influence of local icosahedral order on the nucleation barrier. *Phys. Rev. Lett.* **90**, 195504 (2003).
11. Schenk, T., Holland-Moritz, D., Simonet, V., Bellissent, R. & Herlach, D. M. Icosahedral short-range order in deeply undercooled metallic melts. *Phys. Rev. Lett.* **89**, 075507 (2002).
12. Jakse, N. & Pasturel, A. Local order of liquid and supercooled zirconium by *ab initio* molecular dynamics. *Phys. Rev. Lett.* **91**, 195501 (2003).
13. Di Cicco, A., Trapananti, A., Faggioni, S. & Filipponi, A. Is there icosahedral ordering in liquid and undercooled metals? *Phys. Rev. Lett.* **91**, 135505 (2003).
14. Stratton, W. G. et al. Aluminum nanoscale order in amorphous $Al_{92}Sm_8$ measured by fluctuation electron microscopy. *Appl. Phys. Lett.* **86**, 141910 (2005).
15. Anikeenko, A. V. & Medvedev, N. N. Polytetrahedral nature of the dense disordered packings of hard spheres. *Phys. Rev. Lett.* **98**, 235504 (2007).
16. Ma, D., Stoica, A. D. & Wang, X. L. Power-law scaling and fractal nature of medium-range order in metallic glasses. *Nat. Mater.* **8**, 30–34 (2009).
17. Dmowski, W., Iwashita, T., Chuang, C. P., Almer, J. & Egami, T. Elastic heterogeneity in metallic glasses. *Phys. Rev. Lett.* **105**, 205502 (2010).
18. Hirata, A. et al. Direct observation of local atomic order in a metallic glass. *Nat. Mater.* **10**, 28–33 (2011).
19. Zhong, L., Wang, J., Sheng, H., Zhang, Z. & Mao, S. X. Formation of monatomic metallic glasses through ultrafast liquid quenching. *Nature* **512**, 177–180 (2014).
20. Ding, J. & Ma, E. Computational modeling sheds light on structural evolution in metallic glasses and supercooled liquids. *npj Comput. Mater.* **3**, 9 (2017).
21. Tanaka, H., Tong, H., Shi, R. & Russo, J. Revealing key structural features hidden in liquids and glasses. *Nat. Rev. Phys.* **1**, 333–348 (2019).
22. Khmicha, A., Sbiaaib, K. & Hasnaouib, A. Structural behavior of tantalum monatomic metallic glass. *J. Non-Cryst. Solids* **510**, 81–92 (2019).
23. Gemma, R., Baben, M., Pundt, A., Kapaklis, V. & Hjörvarsson, B. The impact of nanoscale compositional variation on the properties of amorphous alloys. *Sci. Rep.* **10**, 11410 (2020).
24. Nelson, D. R. & Spaepen, F. Polytetrahedral order in condensed matter. *Solid Stat. Phys.* **42**, 1–90 (1989).
25. Sheng, H. W., Luo, W. K., Alamgir, F. M., Bai, J. M. & Ma, E. Atomic packing and short-to-medium-range order in metallic glasses. *Nature* **439**, 419–425 (2006).
26. Cheng, Y. Q. & Ma, E. Atomic-level structure and structure–property relationship in metallic glasses. *Prog. Mater. Sci.* **56**, 379–473 (2011).
27. Chen, M. W. A brief overview of bulk metallic glasses. *NPG Asia Mater.* **3**, 82–90 (2011).
28. Luo, W. K. et al. Icosahedral short-range order in amorphous alloys. *Phys. Rev. Lett.* **92**, 145502 (2004).
29. Hirata, A. et al. Geometric frustration of icosahedron in metallic glasses. *Science* **341**, 376–379 (2013).
30. Shechtman, D., Blech, I., Gratias, D. & Cahn, J. Metallic phase with long-range orientational order and no translational symmetry. *Phys. Rev. Lett.* **53**, 1951–1953 (1984).
31. Levine, D. & Steinhardt, P. J. Quasicrystals: a new class of ordered structures. *Phys. Rev. Lett.* **53**, 2477–2480 (1984).
32. Miao, J., Ercius, P. & Billinge, S. J. L. Atomic electron tomography: 3D structures without crystals. *Science* **353**, aaf2157 (2016).
33. Scott, M. C. et al. Electron tomography at 2.4-ångström resolution. *Nature* **483**, 444–447 (2012).
34. Chen, C. C. et al. Three-dimensional imaging of dislocations in a nanoparticle at atomic resolution. *Nature* **496**, 74–77 (2013).
35. Goris, B. et al. Three-dimensional elemental mapping at the atomic scale in bimetallic nanocrystals. *Nano Lett.* **13**, 4236–4241 (2013).
36. Xu, R. et al. Three-dimensional coordinates of individual atoms in materials revealed by electron tomography. *Nat. Mater.* **14**, 1099–1103 (2015).
37. Haberfehlner, G. et al. Formation of bimetallic clusters in superfluid helium nanodroplets analysed by atomic resolution electron tomography. *Nat. Commun.* **6**, 8779 (2015).
38. Yang, Y. et al. Deciphering chemical order/disorder and material properties at the single-atom level. *Nature* **542**, 75–79 (2017).
39. Zhou, J. et al. Observing crystal nucleation in four dimensions using atomic electron tomography. *Nature* **570**, 500–503 (2019).
40. Tian, X. et al. Correlating the three-dimensional atomic defects and electronic properties of two-dimensional transition metal dichalcogenides. *Nat. Mater.* **19**, 867–873 (2020).
41. Kim, B. H. et al. Critical differences in 3D atomic structure of individual ligand-protected nanocrystals in solution. *Science* **368**, 60–67 (2020).

42. Yang, Y. et al. Determining the three-dimensional atomic structure of an amorphous solid. *Nature* **592**, 60–64 (2021).
43. Egami, T. & Billinge, S. J. L. *Underneath the Bragg Peaks: Structural Analysis of Complex Materials* 2nd edn, Vol. 16 (Pergamon Materials Series, Pergamon-Elsevier Science, 2012).
44. Lechner, W. & Dellago, C. Accurate determination of crystal structures based on averaged local bond order parameters. *J. Chem. Phys.* **129**, 114707 (2008).
45. Lee, G. W. et al. Difference in icosahedral short-range order in early and late transition metal liquids. *Phys. Rev. Lett.* **93**, 037802 (2004).
46. Hales, T. C. A proof of the Kepler conjecture. *Ann. Math.* **162**, 1065–1185 (2005).
47. Plimpton, S. Fast parallel algorithms for short-range molecular dynamics. *J. Comput. Phys.* **117**, 1–19 (1995).
48. Tang, C. & Harrowell, P. Anomalously slow crystal growth of the glass-forming alloy CuZr. *Nat. Mater.* **12**, 507–511 (2013).
49. Ohring, M. *Materials Science of Thin Films* 2nd edn (Academic Press, 2001).
50. Liu, A. J. & Nagel, S. R. Jamming is not just cool any more. *Nature* **396**, 21–22 (1998).
51. Kelton, K. F. & Greer, A. L. *Nucleation in Condensed Matter: Applications in Materials and Biology* (Pergamon, 2010).
52. Debenedetti, P. G. & Stillinger, F. H. Supercooled liquids and the glass transition. *Nature* **410**, 259–267 (2001).

Methods

Physical vapour deposition of amorphous Ta thin films. Ta thin films were prepared in the ultra-high vacuum system associated with the SPLEEM (spin-polarized low-energy electron microscope) instrument at the National Center for Electron Microscopy of the Molecular Foundry at Lawrence Berkeley National Laboratory. Prior to sample growth, Si_3N_4 window grids were cleaned by heating to about 700 K in ultra-high vacuum. For film depositions, the grids were held in a liquid nitrogen cryostat, where tests using Pt1000 sensors indicated that the temperature of the grids remained in the range of 130–150 K during the depositions. High-purity physical vapour beams were produced by heating small charges of Ta in a water-cooled electron beam evaporator and depositing on the Si_3N_4 windows to grow amorphous Ta films. The growth chamber has a base pressure in the 10^{-11} torr range, and during sample deposition, pressure did not exceed the low 10^{-9} torr range. Growth rates were calibrated by growing test films on single crystal Ru(0001), W(110) and Cu(100) substrates while observing low-energy electron reflectivity oscillations, associated with monolayer-by-monolayer epitaxial growth, as well as by measuring peak height ratios in Auger electron spectra of the test samples. All samples were deposited using growth rates in the range of 0.2–1.0 atomic monolayer per minute (or about 2–10 nm h^{-1}). After finishing deposition, all samples were coated with ~2 nm amorphous carbon, deposited from another electron beam evaporator to protect the amorphous structure.

Synthesis of amorphous Pd nanoparticles. The amorphous Pd nanoparticles were synthesized by following a previously reported heating method with a minor modification[53,54]. Typically, 407 mg palladium (II) acetylacetonate, 4 ml trioctylphosphine and 40 ml oleylamine were placed into a round-neck flask. The mixture was degassed at room temperature for 1 hour under vacuum. The reaction solution was then slowly heated to 280 °C (approximately 3 °C min^{-1}) under nitrogen and kept at 280 °C for 30 min. The reaction was quenched by removing the heating mantle and blowing cool air. The product was purified through centrifugation after precipitation with ethanol, and the resulting Pd nanoparticles were redispersed in toluene. The procedure of ligand exchanges with NH_2^- was as follows[55]: 20 mg of $NaNH_2$ was dissolved in 10 ml dimethyl sulfoxide (DMSO), followed by an addition of 10 ml of the Pd nanoparticle toluene solution (0.4 mg ml^{-1}). The mixture was stirred for two days to complete the ligand exchange. The product was collected by centrifugation and washed by acetone one more time. The purified product was obtained by centrifugation and dispersed in nanopore water. Acetone, toluene, DMSO, oleylamine (70%), palladium (II) acetylacetonate (98%), sodium amide ($NaNH_2$, 95%) and trioctylphosphine (97%) were obtained from Sigma-Aldrich.

ADF-STEM data acquisition. Tomographic tilt series of the Ta thin film and Pd nanoparticles were acquired using the TEAM I microscope at the National Center for Electron Microscopy. The microscope was operated in ADF mode with an electron energy of 300 keV (Supplementary Table 1). A low-exposure acquisition scheme was adopted for our data acquisition[34]. When measuring an image at a tilt angle, a nearby nanoparticle or a feature in the Ta film was used to align and focus the image, thus reducing the unnecessary electron dose to the sample under study. At each tilt angle, three sequential images were taken with a dwell time of 3 µs to minimize the dose rate and drift distortion in each image. To further mitigate the beam damage to the samples, the total electron dose of each tilt series was optimized to be about $3.4–6.0 \times 10^5$ electrons $Å^{-2}$ (Supplementary Table 1). With carefully designed sample preparation and data acquisition protocols, our samples were more stable under the electron beam than some of the previously studied glass samples[56,57]. Images taken at 0° tilt angle before, during and after the tilt series indicate that structural change of the samples throughout the experiment was minimal (Supplementary Fig. 4).

Electron diffraction experiments and analysis of the amorphous Ta film and Pd nanoparticles. The electron diffraction patterns of the Ta thin film and Pd nanoparticles were acquired using a Thermo Fischer Themis transmission electron microscope equipped with a Ceta 2 camera (insets in Supplementary Fig. 5a,c). The accelerating voltage was 300 kV and a 10 µm aperture was used to select a desired area, from which the diffraction patterns were collected with the central beam blocked by a beam stop. To calculate the structure factor from each diffraction pattern, a mask was generated to remove the beam stop by properly thresholding the intensity. By fitting the first diffraction ring, the centre of the diffraction pattern was identified and the radially averaged intensity was obtained. A gold sample was used as a reference to calibrate the reciprocal space unit, yielding the intensity distribution as a function of the spatial frequency, $I(q)$. The structure factor, $S(q)$, was computed from $I(q)$ by using the SUePDF software[58], where the atomic form factor was set by properly selecting the chemical species and electron energy. The background was optimized by specifying the pre-peak and the tail location of $I(q)$, the number of middle reference points and the maximum fitting order. Proper parameters were selected during this step to ensure that the resulting $S(q)$ oscillates and converges to unity at large q (Supplementary Fig. 5a,c). The PDF was computed by taking the Fourier transform of $S(q)$. For a diffraction pattern with a high signal-to-noise ratio, its reduced PDF has a linear dependence near the origin, from the slope of which the atomic density can be extracted[43,59]. But our samples are thin (≤10 nm) and the diffraction patterns do not have a sufficiently high signal-to-noise ratio, resulting in some oscillations at low spatial frequency. To correct for the oscillations, SUePDF was used to normalize the reduced PDF by fitting a straight line from the origin to the left valley of the first peak, from which the final PDF was obtained (Supplementary Fig. 5b,d).

Image preprocessing. The following four steps were used to perform image preprocessing.

(1) Drift correction[36]. To correct sample drift, three ADF-STEM images at each tilt angle were registered using the following procedure. First, a region of 400×400 pixels from the second and third images was cropped and scanned over the first one with a step size of 0.05 pixel. Next, the cross-correlation coefficient between images was calculated, where the relative drift vectors were identified by the maximum cross-correlation. The ADF-STEM images have a typical drift of less than 1 pixel. We then applied drift distortion correction to each image along the slow scan direction. By assuming a linear drift during the data acquisition, the drift for each pixel in the image can be determined and corrected by interpolating the raw image with drift-corrected pixel positions. Finally, the three drift-corrected images at each tilt angle were averaged for denoising.

(2) Image denoising. The experimental images have both Poisson and Gaussian noise. A general algorithm named block-matching and 3D filtering (BM3D)[60] has been proven effective in previous AET experiments[36,38,39] and was applied to denoise the drift-corrected images. To optimize the BM3D parameters, we first estimated the Gaussian and Poisson noise in the experimental images and then applied BM3D to denoise a simulated ADF-STEM image with the same noise level by varying denoising parameters. The best parameters were identified by maximizing the cross-correlation between the denoised image and the simulated noise-free image. These optimized parameters were used to denoise all the experimental images.

(3) Background subtraction. For each denoised image, a mask slightly larger than the sample was generated by thresholding. From the background outside the mask, the background level within the mask was estimated using Laplacian interpolation[42]. The estimated background was subtracted from the denoised image.

(4) Image alignment. The images in each tilt series were aligned using the following procedure. The tilt series of the two Pd nanoparticles was aligned by the centre of mass and common line method, as described in previous AET experiments[33,34]. For the Ta thin film, we first performed a pre-alignment by using cross-correlation between the images of neighbouring tilt angles. Next, based on reference markers in the sample (in this case we chose an isolated region as the reference marker), we used the common line method and the centre of mass[33,34] to align the thin film along the tilt axis and perpendicular to the tilt axis, respectively. We repeated this alignment process until no further improvement could be made.

A 3D reconstruction with the RESIRE algorithm. After image preprocessing, each experimental tilt series was computed by the Real Space Iterative Reconstruction (RESIRE) algorithm[42]. The algorithm minimizes the difference between the experimental and computed images using the gradient descent method. The error function and the gradient are defined as

$$\varepsilon_\theta(O) = \frac{1}{2}\sum_{x,y} |\Pi_\theta(O)\{x,y\} - b_\theta\{x,y\}|^2 \quad (1)$$

$$\nabla\varepsilon_\theta(O)\{u,v,w\} = \Pi_\theta(O)\{x,y\} - b_\theta\{x,y\} \text{ where } \begin{bmatrix} u \\ v \\ w \end{bmatrix} = R_\theta \begin{bmatrix} x \\ y \\ z \end{bmatrix} \text{ for some } z \quad (2)$$

where ε_θ is the error function of a 3D object (O) at tilt angle θ, $\prod_\theta(O)$ calculates the projection of the object at angle θ, b_θ is the experimental image at angle θ, and $\{x, y, z\}$ are the coordinates, ∇ is the gradient and R_θ is the rotation matrix transforming coordinates $\{x, y, z\}$ to $\{u, v, w\}$. More mathematical description of RESIRE and its superior performance to other algorithms will be presented in a follow-up paper.

The two Pd nanoparticles were directly reconstructed by RESIRE. For the Ta thin film, we first performed a large volume reconstruction with RESIRE. After estimating the thickness variation of the Ta thin film, we applied scanning AET to do multiple local volume reconstructions and then patched them together to obtain a full reconstruction[40]. Previous study has shown that scanning AET can improve the reconstruction of 2D layered and thin-film samples over AET[40].

From the 3D reconstructions of the Pd nanoparticles and Ta film, we performed angular refinement and image alignment until the results converged. Next, we traced and refined the 3D atomic coordinates from each reconstruction (see the section below), from which reference images were calculated at the

corresponding tilt angles. The experimental tilt angles and images were further refined and realigned using these reference images. After these procedures, the final reconstructions were performed for all three samples.

Determination and refinement of 3D atomic coordinates. From the reconstructions of the Pd nanoparticles and the Ta thin film, we determined their 3D atomic coordinates using the following steps.

(1) We interpolated each reconstruction onto a finer grid with three times oversampling using the spline method. All the local maxima in the reconstruction were identified, and the positions of potential atoms were extracted from a local volume of 0.8 Å × 0.8 Å × 0.8 Å with a polynomial fitting method[39,61]. For every potential atom, a minimum distance of 2 Å to its neighbouring atoms has to be satisfied. This constraint is based on the fact that all the interatomic distances in our samples are larger than 2 Å. After iterating through all local maxima, a list of potential atoms was obtained.
(2) To separate non-atoms from the potential atoms, we employed the K-mean clustering method[38,39,62] based on the integrated intensity of a local volume (0.8 Å × 0.8 Å × 0.8 Å) around each potential atom position. After excluding non-atoms, the potential atomic models of the two Pd nanoparticles and Ta film were obtained.
(3) By carefully comparing the individual atomic positions in the potential atomic models with the 3D reconstructions, we manually corrected a very small fraction (typically <1%) of unidentified or misidentified atoms. Note that manual correction of a very small fraction of atoms is routinely used in macromolecular crystallography for atom tracing and refinement[63].
(4) We repeated steps (2) and (3) until no further improvement could be made, resulting in the 3D atomic models of the three amorphous materials.
(5) The 3D atomic coordinates in each model were refined by minimizing the error between the experimental and computed images using the gradient descent as described elsewhere[36,38,39]. The refinement results are shown in Supplementary Table 1.

The 3D precision estimation. To estimate the 3D precision of our method, we performed multi-slice simulations[64,65] to calculate ADF-STEM images from the Ta atomic model using the same experimental parameters specified in Supplementary Table 1. A tilt series of 46 multi-slice images was computed at the experimental tilt angles. To account for the electron probe size and other effects, the image was convolved with a Gaussian function. A representative multi-slice ADF-STEM image at 0° tilt angle is shown in Supplementary Fig. 6b, which is in good agreement with the corresponding experimental image (Supplementary Fig. 6a). From the 46 multi-slice ADF-STEM images, we used the same reconstruction, tracing and refinement procedure to obtain a new 3D atomic model. By comparing the new atomic model with the experimental one, we found that 98.1% of the atoms are identical, with a root-mean-square deviation of 18 pm (Supplementary Fig. 6c).

Calculation of the PDF from the experimental 3D atomic model. The following procedure was used to calculate the PDF from the experimental atomic model of each sample[59]. (1) The histogram of atom pair distances in spherical shells was computed with a shell thickness of 0.1 Å. (2) The counts in each spherical shell were divided by the volume of the spherical shell, yielding the density of atom pairs as a function of the pair distance. (3) The PDF was scaled to approach one at large pair distances. Using this procedure, we calculated the PDFs of all the atoms in the Ta thin film and two Pd nanoparticles. From the PDF of each material, we determined the first valley position, corresponding to the first-nearest-neighbour shell distance. This distance was used to compute the local bond orientational order (BOO) parameters (see the section below), from which crystal nuclei were identified. After excluding the crystal nuclei, the PDFs of the disordered atoms in the amorphous materials were recalculated, shown in Fig. 1c.

The local BOO parameters. We calculated the averaged local BOO parameters (Q_4 and Q_6) to quantify the disorder of the amorphous materials[44,66]. The Q_4 and Q_6 values were computed based on the procedure published elsewhere[44], where the first-nearest-neighbour shell distance (Fig. 1c) was used as a constraint. The Q_4 and Q_6 were used to calculate the normalized BOO parameter, defined as $\sqrt{Q_4^2+Q_6^2}/\sqrt{Q_{4\,\mathrm{fcc}}^2+Q_{6\,\mathrm{fcc}}^2}$, where $Q_{4\,\mathrm{fcc}}$ and $Q_{6\,\mathrm{fcc}}$ are the reference values of the face-centred cubic (fcc) lattice. We separated crystal nuclei from amorphous structure by setting the normalized BOO parameter larger than or equal to 0.5 (ref. [42]; red dashed lines in Supplementary Fig. 8a–c).

The Voronoi tessellation, coordination number and local mass density distribution. The Voronoi tessellation of each 3D atomic model was calculated by following a procedure published elsewhere[4]. To characterize the nearest-neighbour atoms around each centre atom, a regulation was applied to each Voronoi polyhedron where neighbouring atoms with the facet area less than 1% of the total Voronoi surface area were removed during the analysis[25]. All the Voronoi polyhedra were then indexed by n_3, n_4, n_5 and n_6 with n_i denoting the number of i-edged faces. The coordination number was calculated by $\sum_i n_i$.

The mass density for each atom was calculated by dividing the atomic mass by its atomic volume, which is defined as the volume of its Voronoi polyhedron without regulation. The densities at all atomic positions were interpolated onto a 3D grid and then convolved with a Gaussian kernel. The width of the Gaussian kernel was set as the first-nearest-neighbour shell distance defined by the PDF. Using this procedure, we obtained the local mass density distribution of the three amorphous materials (Fig. 3 and Supplementary Fig. 10).

Polytetrahedral packing analysis. To identify all the tetrahedra in each amorphous material, we used the distortion parameter (δ) defined in the main text, where the maximum edge length of each tetrahedron cannot be larger than the first-nearest-neighbour shell distance (Fig. 1c). In the polytetrahedral packing analysis, we set δ to be the maximum allowed distortion parameter to identify each tetrahedron. The population of the tetrahedra strongly depends on δ. With $\delta > 0.2$, more than 96.8% of the atoms in the three amorphous materials form tetrahedra (green curves in Supplementary Fig. 9). From these tetrahedra, we searched for polytetrahedral motifs and found four main motifs (Fig. 2a): (1) triplets with three face-sharing tetrahedra (but the first and third tetrahedra do not share a face); (2) quadrilateral bipyramids with four face-sharing tetrahedra; (3) pentagonal bipyramids with five face-sharing tetrahedra; and (4) hexagonal bipyramids with six face-sharing tetrahedra. All these four polytetrahedral motifs share two capping atoms (brown atoms in Fig. 2a). Although we observed other motifs in the amorphous materials, their population is much smaller than that of the four main motifs. We represented the four main motifs by three-, four-, five- and six-fold skeletons, which connect the centroids of the tetrahedra (Fig. 2a). The fraction of the four main motifs, defined as the number of tetrahedra in each motif divided by the total number of tetrahedra in each amorphous material, strongly depends on δ (Supplementary Fig. 9). The sum of the fraction of the four main motifs can be larger than one because some tetrahedra are overlapped among different motifs. By choosing $\delta \leq 0.255$ (refs. [15,46]), we found that the polytetrahedral packing of the four motifs is strongly correlated with the local mass density heterogeneity (Fig. 3 and Supplementary Fig. 10).

PBNs. We searched for the PBNs in each amorphous material using the following procedure. (1) From the polytetrahedral packing of the sample, we only kept pentagonal bipyramids, which are represented by five-fold skeletons. (2) We started a PBN by choosing a five-fold skeleton and identifying all its edge-sharing skeletons. (3) We repeated step (2) until all the edge-sharing skeletons in the PBN were found. (4) We started a new PBN and repeated the procedure. (5) After identifying all the PBNs in the sample, we kept only those PBNs with five or more pentagonal bipyramids. The five largest PBNs in the Ta thin film, two Pd nanoparticles and MD-simulated Ta liquid (5,200 K) are shown in Supplementary Figs. 16–18 and 20. The PBN size is defined as the number of pentagonal bipyramids in the network. The PBN length was measured along the longest direction of the network (Supplementary Fig. 15). We used the same procedure to find the quadrilateral and hexagonal bipyramid networks in each amorphous material.

MD simulations. To understand our experimental observations, we performed MD simulations of a Ta bulk system using the large-scale atomic/molecular massively parallel simulator package[47]. The system consisted of 31,250 atoms using the embedded-atom-method interatomic potential[19] with periodic boundary conditions. The system was melted and equilibrated at 5,200 K before quenching the system at a cooling rate of 10^{13} K s^{-1} using the isothermal–isobaric ensemble. The polytetrahedral packing analysis was performed on atomic configurations throughout the quench process, and we observed similarities between the experimental amorphous materials and the MD simulations of liquids. This realistic interatomic potential was chosen for three reasons. First, the interatomic potential was developed with a focus on the metallic glass and liquid phases. Second, the simulated metallic glass structure factors correlate well with the experimental data[19]. Third, the simulated liquid phase PDF has the lowest least-square fitting error to the experimental Ta PDF (Fig. 1c) compared to other potentials[67,68], although all these interatomic potentials show similar PBNs and trends through the glass transition.

Quantifying the crystalline–amorphous interface. We quantified the characteristic width of the crystalline–amorphous interface using the normalized BOO parameter. In each sample, the 3D surface of every nucleus was determined by setting the normalized BOO parameter larger than or equal to 0.5. The perpendicular distance of atoms to the 3D surface of the nucleus was calculated, where the atoms outside and inside the surface have a positive and negative distance, respectively. By averaging all the nuclei in each sample, we obtained the distribution of the normalized BOO parameter as a function of the perpendicular distance to the surface of the crystal nuclei (blue circles in Supplementary Fig. 22). To extract the characteristic width (d_c) of the crystalline–amorphous interface, the experimental data points were fitted with an exponential decay function $y = ae^{-x/d_c} + b$ (solids curves in Supplementary Fig. 22), where a and b are two constants. The characteristic width of the crystalline–amorphous interface was determined to be 3.0, 4.2 and 4.3 Å for the Ta film and Pd_1 and Pd_2 nanoparticles, respectively, values that agree with the previous MD simulation result[48].

Data availability

The raw and processed experimental data are available at https://github.com/AET-AmorphousMaterials/Supplementary-Data-Codes. The 3D atomic coordinates of the Ta thin film and Pd_1 and Pd_2 nanoparticles have been deposited in the Materials Data Bank (www.materialsdatabank.org) with Materials Data Bank identification numbers TaXX00001, PdXX00001 and PdXX00002, respectively.

Code availability

The MATLAB source codes for the RESIRE reconstruction and data analysis used in this work are available at https://github.com/AET-AmorphousMaterials/Supplementary-Data-Codes.

References

53. Liu, Y. et al. Surfactant-induced postsynthetic modulation of Pd nanoparticle crystallinity. *Nano Lett.* **11**, 1614–1617 (2011).
54. Kim, S.-W. et al. Synthesis of monodisperse palladium nanoparticles. *Nano Lett.* **3**, 1289–1291 (2003).
55. Nag, A. et al. Metal-free inorganic ligands for colloidal nanocrystals: S^{2-}, HS^-, Se^{2-}, HSe^-, Te^{2-}, HTe^-, TeS_3^{2-}, OH^-, and NH_2^- as surface ligands. *J. Am. Chem. Soc.* **133**, 10612–10620 (2011).
56. Zheng, K. et al. Electron-beam-assisted superplastic shaping of nanoscale amorphous silica. *Nat. Commun.* **1**, 24 (2010).
57. Cao, C. R. et al. Liquid-like behaviours of metallic glassy nanoparticles at room temperature. *Nat. Commun.* **10**, 1966 (2019).
58. Tran, D. T., Svensson, G. & Tai, C. W. *SUePDF*: a program to obtain quantitative pair distribution functions from electron diffraction data. *J. Appl. Crystallogr.* **50**, 304–312 (2017).
59. Billinge, S. J. L. The rise of the X-ray atomic pair distribution function method: a series of fortunate events. *Phil. Trans. R. Soc. A* **377**, 20180413 (2019).
60. Dabov, K., Foi, A., Katkovnik, V. & Egiazarian, K. Image denoising by sparse 3-D transform-domain collaborative filtering. *IEEE Trans. Image Process.* **16**, 2080–2095 (2007).
61. Rogers, S. S., Waigh, T. A., Zhao, X. & Lu, J. R. Precise particle tracking against a complicated background: polynomial fitting with Gaussian weight. *Phys. Biol.* **4**, 220–227 (2007).
62. Lloyd, S. Least squares quantization in PCM. *IEEE Trans. Inf. Theory* **28**, 129–137 (1982).
63. Brünger, A. T. et al. Crystallography & NMR System: a new software suite for macromolecular structure determination. *Acta Crystallogr. D* **54**, 905–921 (1998).
64. Ophus, C. A fast image simulation algorithm for scanning transmission electron microscopy. *Adv. Struct. Chem. Imag.* **3**, 13 (2017).
65. Pryor, A., Ophus, C. & Miao, J. A streaming multi-GPU implementation of image simulation algorithms for scanning transmission electron microscopy. *Adv. Struct. Chem. Imag.* **3**, 15 (2017).
66. Steinhardt, P. J., Nelson, D. R. & Ronchetti, M. Bond-orientational order in liquids and glasses. *Phys. Rev. B* **28**, 784–805 (1983).
67. Ravelo, R., Germann, T. C., Guerrero, O., An, Q. & Holian, B. L. Shock-induced plasticity in tantalum single crystals: interatomic potentials and large-scale molecular-dynamics simulations. *Phys. Rev. B* **88**, 134101 (2013).
68. Purja Pun, G. P., Darling, K. A., Kecskes, L. J. & Mishin, Y. Angular-dependent interatomic potential for the Cu–Ta system and its application to structural stability of nano-crystalline alloys. *Acta Mater.* **100**, 377–391 (2015).

Acknowledgements

We thank J. Ciston for help with data acquisition and X. Tian for help with data analysis. This work was primarily supported by the US Department of Energy, Office of Science, Basic Energy Sciences, Division of Materials Sciences and Engineering under award no. DE-SC0010378. We also thank the support by STROBE: a National Science Foundation Science and Technology Center under award no. DMR-1548924. Some of the data analysis was partially supported by the National Science Foundation Designing Materials to Revolutionize and Engineer our Future (DMREF) programme under award no. DMR-1437263 and the Army Research Office Multidisciplinary University Research Initiative (MURI) programme under grant no. W911NF-18-1-0431. The ADF-STEM imaging with TEAM I was performed at the Molecular Foundry, which is supported by the Office of Science, Office of Basic Energy Sciences of the US Department of Energy under contract no. DE-AC02-05CH11231.

Author contributions

J.M. conceived the idea and directed the project; A.K.S. synthesized the amorphous Ta thin film; Y.N. and O.C. synthesized the amorphous Pd nanoparticles; J.Z., A.K.S., P.E. and J.M. discussed and performed the AET experiments of the amorphous materials; and M.P., Y. Yuan, S.J.O. and J.M. developed the 3D reconstruction algorithm. Y. Yuan, D.S.K., D.J.C., F.Z., Y. Yang and J.M. performed image reconstruction and atom tracing, analysed the data and interpreted the results; D.S.K. and J.M. discussed and performed the MD simulations. Y. Yuan, D.S.K. and J.M. wrote the manuscript. All authors commented on the manuscript.

Competing interests

The authors declare no competing interests.

Additional information

Supplementary information The online version contains supplementary material available at https://doi.org/10.1038/s41563-021-01114-z.

Correspondence and requests for materials should be addressed to Jianwei Miao.

Peer review information *Nature Materials* thanks Matthew Kramer and Yong Yang for their contribution to the peer review of this work.

Reprints and permissions information is available at www.nature.com/reprints.